Cryo-EM reconstruction of helical polymers: Beyond the simple cases

Mark A.B. Kreutzberger[‡] ⬛, Ravi R. Sonani[‡] ⬛ and Edward H. Egelman ⬛

Department of Biochemistry and Molecular Genetics, University of Virginia Medical School, Charlottesville, VA, USA

Corresponding author:
Edward H. Egelman;
Email: egelman@virginia.edu

[‡]These authors contributed equally

Abstract

Helices are one of the most frequently encountered symmetries in biological assemblies. Helical symmetry has been exploited in electron microscopic studies as a limited number of filament images, in principle, can provide all the information needed to do a three-dimensional reconstruction of a polymer. Over the past 25 years, three-dimensional reconstructions of helical polymers from cryo-EM images have shifted completely from Fourier–Bessel methods to single-particle approaches. The single-particle approaches have allowed people to surmount the problem that very few biological polymers are crystalline in order, and despite the flexibility and heterogeneity present in most of these polymers, reaching a resolution where accurate atomic models can be built has now become the standard. While determining the correct helical symmetry may be very simple for something like F-actin, for many other polymers, particularly those formed from small peptides, it can be much more challenging. This review discusses why symmetry determination can be problematic, and why trial-and-error methods are still the best approach. Studies of many macromolecular assemblies, such as icosahedral capsids, have usually found that not imposing symmetry leads to a great reduction in resolution while at the same time revealing possibly interesting asymmetric features. We show that for certain helical assemblies asymmetric reconstructions can sometimes lead to greatly improved resolution. Further, in the case of supercoiled flagellar filaments from bacteria and archaea, we show that the imposition of helical symmetry can not only be wrong, but is not necessary, and obscures the mechanisms whereby these filaments supercoil.

Table of contents

Introduction

Symmetry is ubiquitous in biology, and viruses provide some of the simplest models for understanding how multiple copies of the same protein can be assembled into large macromolecular assemblies. In an extremely speculative paper with little data to support their argument, Watson and Crick suggested almost 70 years ago why all small viruses are either rod-like or spherical (Crick and Watson, 1956): the rod-like viruses would have helical symmetry, while the spherical ones would have a point-group symmetry, with icosahedral symmetry being one of the three possibilities they considered. Many years of subsequent investigations have amply confirmed this speculation, and atomic structures now exist for hundreds of helical and icosahedral viruses. However, detailed studies of bacterial, archaeal, and eukaryotic cells have also shown how multiple copies of the same protein can be assembled symmetrically into shells, rings, and filaments. This review will focus on using cryo-EM to study the filaments and tubes assembled by viruses, bacteria, archaea, and eukaryotes, understanding the helical symmetry present and how helical symmetry may be broken in some of these systems. The review will also discuss some of the work being done using peptides and other relatively small molecules that self-assemble into tubes and filaments. In all cases, the

tremendous advances that have been made in cryo-EM over the past 12 years, referred to as the 'resolution revolution' (Kuhlbrandt, 2014), allow for the atomic structures of these assemblies to be readily determined. This review will most definitely not attempt to summarize the ~1,800 volumes currently deposited in the Electron Microscopy Data Bank (EMDB) that have been reconstructed with helical symmetry, nor will it attempt to be a complete handbook for how to process cryo-EM images of helical structures. Rather, it will focus on a relatively few issues and problems that arise from such polymers.

The first three-dimensional reconstruction by electron microscopy was of a helical bacteriophage tail (DeRosier and Klug, 1968). Many more such structures have now been solved and at ever increasing resolutions. Some of the 'model' systems that have played an important role in the general development of cryo-EM include cytoskeletal filaments such as actin (Fujii et al., 2010; Merino et al., 2018) and microtubules (Alushin et al., 2014; Zhang et al., 2015). Of the ~1,800 cryo-EM volumes currently deposited in the EMDB that have been solved by helical reconstruction, the largest single-family certainly involves amyloid. It is far beyond the scope of this article to discuss these structures or the particular methodological problems that they pose (Lovestam and Scheres, 2022), but several recent papers provide some overview (Garcia-Pardo and Ventura, 2024; Mishra, 2023; Scheres et al., 2023). There is an expanding body of literature about enzymes that self-assemble into helical polymers, discussed and reviewed in a number of papers (Hvorecny and Kollman 2023; Lynch et al., 2020; Park and Horton 2019; 2020; Pillay et al., 2022). While some of the earliest observations of filamentation by an enzyme, such as glutamine synthetase, date from 1968 (Valentine et al., 1968), the acetyl CoA carboxylase story followed soon after (Kleinschmidt et al., 1969). Remarkably, it has been shown that filamentation can be used to either repress enzymatic activity or activate it! It is quite likely that the repertory of enzymes that polymerize will continue to grow, as judged by a recent finding of an extracellular serine peptidase Vpr from *Bacillus* forming enzymatically active filaments (Cheng et al., 2023).

Helical symmetry

Helical symmetry, in crystallographic terms, is a screw symmetry where there is a coupled rotation about the helical axis and translation along the helical axis relating identical objects. A helical filament or tube can have an additional rotational point group symmetry C_n, where a rotation of the structure about the helical axis by 360°/n leaves the structure invariant. Further, there can be a dyad axis perpendicular to the helical axis such that rotation of the structure around this dyad axis by 180° leaves the structure invariant. Since we are dealing in this review with biological polymers (composed primarily of proteins and peptides) where the building blocks are intrinsically asymmetric, a filament or tube with dyadic symmetry must have an asymmetric unit that is at least a dimer, so that the asymmetric unit itself has dyadic symmetry. The dyadic symmetry, D_1, can be combined with a C_n point group symmetry to give a D_n symmetry in addition to the screw symmetry. In a three-dimensional crystal, the only screw symmetries that are possible have either 2, 3, 4 or 6 subunits per turn allowing all subunits to be in identical environments. Perhaps as a consequence, the screw symmetry was described in historical papers (Cochran, 1951; Klug et al., 1958) as involving the ratio of integers (e.g., tobacco mosaic virus was a 49/3 helix having 49 subunits in 3 turns), but we now understand that there is no reason for this symmetry outside of a crystal to be described or approximated by integer ratios (Egelman, 2007, 2010).

In the absence of a point group symmetry, the description of the helical symmetry is quite simple. There is a 1-start helix that passes through every subunit, and the pitch of this helix is defined by the number of subunits per turn (which is 360° divided by the rotation per subunit) times the rise per subunit. The '1-start' description refers to the fact that a plane perpendicular to the filament axis will only intersect this helical line once, while for a 2-start helix such a plane will intersect these helical lines twice, a 3-start three times, and so forth However, there will be potential ambiguities in defining this 1-start helix. For example, if we imagine that F-actin filaments (Figure 1) have 2.16 subunits/turn along a left-handed helix (a rotation of 166.67°), and that the rise per subunit is 27.3 Å, there will be a left-handed 1-start helix with a pitch of 59 Å, but there will also be a right-handed 1-start helix with 1.86 subunits/

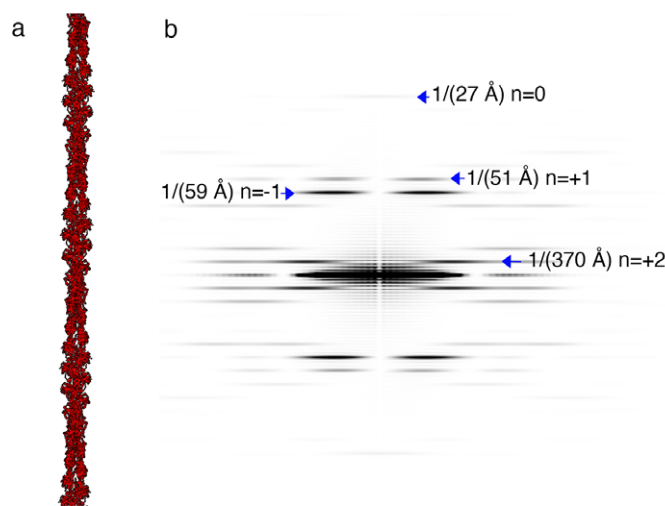**Figure 1.** A simple example of helical symmetry provided by F-actin. (a) A ribbon model of an actin filament (PDB 6DJO). The clear periodicity of 'crossovers' of the two strands (the narrow regions) have a spacing of ~370 Å. (b) The power spectrum generated from a projection of the atomic model. Four layer lines are annotated with their height (the distance from the equator) and their Bessel order.

turn (a rotation of 193.33°) with a pitch of 51 Å. The convention has usually been to define the structure by the 1-start helix having the rotation less than 180°, so in this case we define actin by the left-handed 1-start helix. However, a description using the right-handed 1-start would be just as correct.

Helical reconstruction

Helical reconstruction of filaments using cryo-EM has been thoroughly covered before in previous reviews and papers (Desfosses et al., 2014; Egelman, 2010; 2024; Wang et al., 2022). The software used to reconstruct helical filaments has changed dramatically over the course of the years, but the scheme is basically the same after single-particle approaches to helical reconstruction (Egelman, 2000) have supplanted Fourier-Bessel methods (DeRosier and Klug, 1968; Klug et al., 1958). Currently, helical reconstruction can be performed quite effectively using software packages such as cryoSPARC (Punjani et al., 2017) and RELION (Scheres, 2012). The basic workflow involves the initial processing of micrographs (motion correction, CTF estimation) followed by particle picking (now typically automated). Initial particle sorting can be done using 2D classification, which is the single-particle cryo-EM standard. Following this, the power spectrum should be calculated from a subset of good particles. These can be either hand-picked particles or particles from good 2D classes in a 2D classification job. As previously discussed (Egelman, 2024; Wang et al., 2006), the power spectrum of an average is not the same as the averaged power spectrum. Thus, one must take the individual segments that are part of a class average, impose the rotations that were used to generate the class average (the translations do not matter, as the power spectrum is invariant under translation, generate the power spectrum of these rotationally aligned segments, and then add them all together). This can now be done easily in cryoSPARC. Determining the helical symmetry for a filament or tube from a power spectrum may be problematic and is often the most difficult part of dealing with helical structures (Egelman, 2024). There are some polymers where the symmetry is completely unambiguous at even relatively low resolution, so it may help the discussion to start with such an example. The second one is much more complicated, and there are ~50 possible solutions. Unfortunately, most real specimens are likely to behave more like the second case than the first one!

A simple case of helical symmetry determination

Figure 1a shows an atomic model of an actin filament, and Figure 1b shows the power spectrum computed from the projection of this filament model. Four layer lines are labeled with their height, and the correct Bessel order is assigned. We will show that at the extremely low resolution of ~35 Å, before one would see the $n = 0$ meridional, corresponding to the rise per subunit, at $1/(27 \text{ Å})$, the symmetry is unambiguous with only three-layer lines visible. The helical symmetry (giving the rise and rotation per subunit) is completely determined if any two of these three-layer lines have a Bessel order correctly assigned. The strongest layer line is the one at $1/(59 \text{ Å})$. We can measure R, the distance of the peak on this layer line from the meridian, and it is ~0.009 Å^{-1}. We can estimate (at low resolution) the diameter of the filament, and it is ~80 Å (but the atomic model is actually ~95 Å in diameter). The argument x for a Bessel function $J_n(x)$ on a layer line will be $x = 2\pi Rr$, where r is the real space radius of an atom, and the first

maximum for a Bessel order 1 will be when $2\pi Rr = 1.84$, while for a Bessel order 2, the first maximum will be when $2\pi Rr = 3.05$. Using $r = 40 \text{ Å}$ and $R = 0.009$ (observables from the image and the power spectrum, respectively), we get an argument of 2.3. This is significantly less than 3.05, establishing that the Bessel order on this $1/(59 \text{ Å})$ layer line could only be either $+1$ or -1. Similarly, we can look at the $1/(51 \text{ Å})$ layer line and measure $R = 0.0085$. This also shows that the Bessel order on the $1/(51 \text{ Å})$ layer line could only be $+1$ or -1. These two layer lines must have the opposite signs, as the vector relating them should have a Bessel order of $+2$ or -2, to give rise to the peak on the layer line at $1/(370 \text{ Å})$. If they had the same sign, then the Bessel order on the $1/(370 \text{ Å})$ layer line would need to be 0, which is clearly not the case. We are thus left with an intrinsic ambiguity about the helical hand from this assignment of Bessel orders, but we can easily resolve it by looking at AFM or metal-shadowed images of actin filaments which show us that the long pitch actin helices giving rise to the $1/(370 \text{ Å})$ layer line are right-handed, so we now know that there is $n = -1$ at $1/(59 \text{ Å})$ and $n = +1$ at $1/(51 \text{ Å})$. Life would be much easier if all helical structures led to such simple solutions.

A difficult case of helical symmetry determination

Helical structures made up of shorter peptides are particularly challenging in terms of helical symmetry determination. Consider the LD-tube (Figure 2) composed of the dipeptide (L,D)-2NapFF (Sonani et al., 2024a). This peptide has a naphthalene moiety attached to the N-terminus of diphenylalanine (FF), with the second phenylalanine being in the D-isoform (Figure 2a). The (L,D)-2NapFF peptide self-assembles to form a ~ 300 Å wide, thin-walled, hollow tube, as evidenced by cryo-EM micrographs and 2D class averages (Figure 2b). The power spectrum of LD-tube segments reveals high-resolution features up to ~3.0 Å, suggesting that the packing of dipeptides is highly ordered. This, at first impression, implies that determining the helical symmetry and solving the structure might be relatively straightforward.

However, the task was more complex than it appears, as there are approximately 50 possible helical symmetries necessitating a testing of each. By knowing the tube's radius (r) and the 'R' value (distance of the first peak of the layer line from the meridian), one can calculate the argument x for a Bessel function $J_n(x)2\pi Rr$ for layer lines ll1 at $1/(21 \text{ Å})$ and ll7 at $1/(3 \text{ Å})$ (Figure 2c). However, it is clear that there is not a single value of r, as the walls of the tube have a finite thickness. So putting in a range of values for r suggests that ll1 could correspond to Bessel orders 27, 28, 29, 30, 31, 32, or 33. But ll7 could be anything from $n = 0$ to $n = 12$. So the number of combinations is at least $7*13 = 91$, without considering the signs of these Bessel orders. Considering the sign, such that each Bessel order can be either positive or negative, there would be 364 possibilities! We know that the absolute hand cannot be determined from the power spectrum (Wang et al., 2022), so we do not need to calculate, for example, both 28/7 and $-28/-7$ for ll1/ll7, as one will simply be the mirror image of the other. We will thus assume that the Bessel order on ll1 is positive. Consequently, there are up to 182 possible helical symmetries, such as Bessel orders for ll1/ll7 being 28/7, 28/-7, 29/7, 29/-7, and so forth. However, ll6 in the power spectrum has a peak substantially closer to the meridian than ll1, and ll6 will be the Bessel order on ll1 subtracted from the Bessel order on ll7. For example, if ll1 is 30 and ll7 is 7, ll6 would be -23, while if ll1 is 30 and ll7 is -7, ll6 would be -37. Assuming that ll1 is a positive Bessel order, then ll7 must also be positive and cannot be
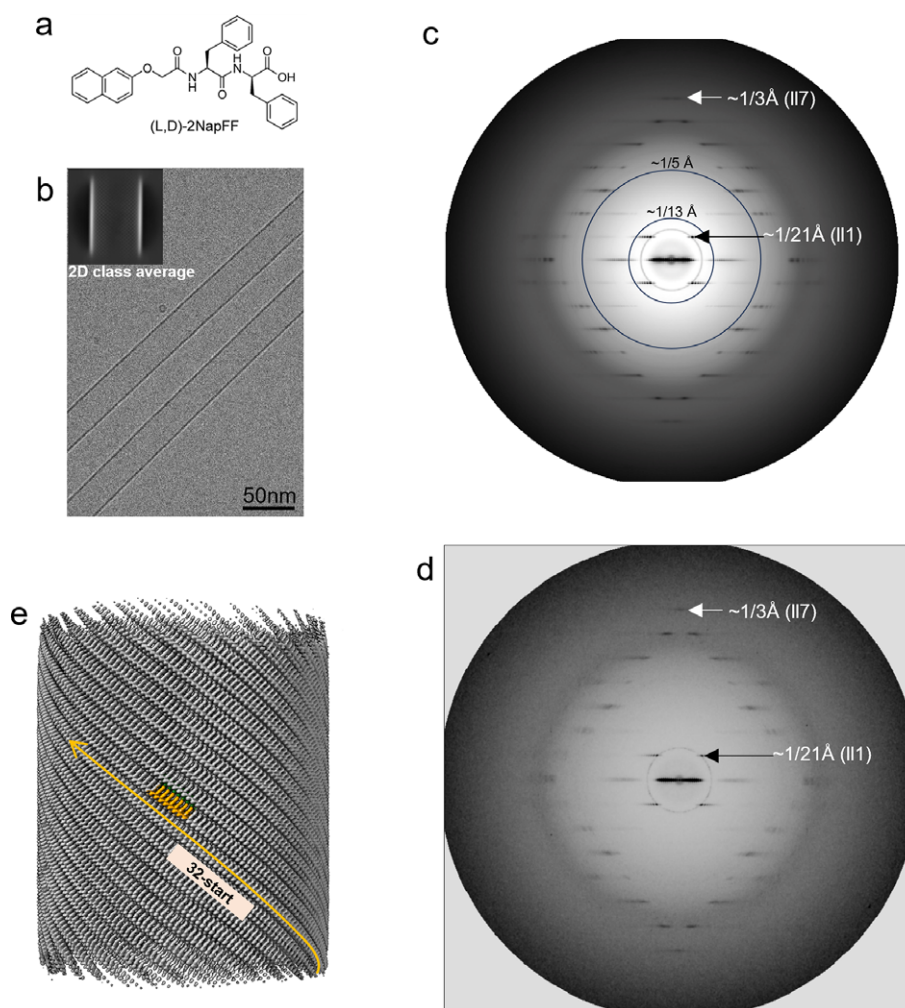
Figure 2. A difficult case of helical symmetry determination. (a) Chemical structure of dipeptide, (ʟ,ᴅ)-2NapFF. (b) Cryo-EM micrograph, and (c) average power spectrum of LD tube – a helical polymer of (ʟ,ᴅ)-2NapFF. (d) Power spectrum of subset of LD tube segments estimated to have a very small out-of-plane tilt of ~2°, giving rise to meridional intensity on the layer line at 1/(3.0 Å). (e) Surface of 3D reconstruction of LD tube showing 32-start helical organization. (Sonani et al., 2024a).

less than 6. This greatly reduces the number of possible solutions to only 49, with ll1 being from 27–33 and ll7 being from 6–12.

Could generating a power spectrum at even higher resolution solve the ambiguities present? If we somehow had layer lines out to 1 Å (as opposed to the ~3 Å we show in Figure 2c) would these ambiguities vanish? The answer is simply no, for the reason that out-of-plane tilt remains an unknown variable and one that we cannot control in specimen preparation. Helical symmetry is most simply understood when filaments are lying in the plane of projection, that is when the helical axis is perpendicular to the electron beam. For negatively stained specimens that have been adsorbed to a substrate, such as a carbon film, this is almost certainly the case. However, in cryo-EM, the ice has a finite thickness, and a filament may not be precisely in a plane perpendicular to the beam. We refer to this as out-of-plane tilt, and it can greatly complicate the analysis of diffraction patterns as intensities on layer lines are shifted (Egelman, 2014).

This is illustrated by the fact that in Figure 2d a power spectrum from a subset of tubes is shown where the layer line at 1/(3 Å) has clear meridional intensity and must be $n = 0$ if there were no out-of-plane tilt. But we know that it is $n = 9$, and the amount of out-of-plane tilt needed to make the $n = 9$ look like an $n = 0$ is only about 2° for this layer line. If we had layer lines beyond the 1/(3 Å)

seen, they would be even more sensitive to out-of-plane tilt, and thus would provide no useful information for determining the helical symmetry.

The problem is further complicated by the fact that closely related symmetries can have axial rises, in some cases, differing by only a few thousandths of an Å. For instance, the helical symmetries 31/9 and 32/9, based on Bessel orders for ll1/ll7, have axial rises of 0.102 Å and 0.0989 Å, respectively. The 0.003 Å difference in axial rise between these symmetries results in very similar helical nets (discussed below), making it challenging to distinguish between them. In practice, this can lead to numerous local minima during refinement, in which the alignment procedure can get stuck.

Additionally, the absence of low-to-medium resolution features, as observed in the power spectrum with no detectable nonequatorial peaks between 1/(13 Å) to 1/(5 Å) (Figure 2c), complicates matters. This absence of low-resolution information, a well-known problem for amyloid filaments, hampers iterative refinement algorithms. The iterative refinement algorithm, used by programs such as Relion and CryoSPARC, requires a reference volume at each cycle for the alignment of the images. The starting volume, for helical refinement, can be a simple cylinder, which gets better at every iteration based on the low to medium-resolution features

present in the structure. Since the LD-tube has no low-resolution features, the iterative approach tends to get stuck in local minima. A solution is to use an initial model. One approach for generating an initial model involves using 2D class averages (Scheres, 2020). This method mainly relies on the apparent crossovers in the 2D class averages of amyloid filaments. However, since no such crossover is visible in 2D class averages of LD tube, this method may not be directly applicable. Alternatively, an initial model can be generated from a small subset of unbinned segments using SPIDER, as described in Sonani et al. (2024a), where random azimuthal angles are assigned to these projections. Starting with such an initial model and by extensive symmetry testing of the 49 possible symmetries, the 3.3 Å map of LD tube was achieved, revealing the 32-start helical organization of dipeptides in the tube (Figure 2e).

Unique cases in helical symmetry

A case with mixed helical symmetries

In the context of problematic cases, helical symmetry determination for a sample exhibiting dual helical symmetries is challenging. The contractile tail of *Myoviridae* bacteriophages comprises a

central tube and surrounding sheath, both of which exhibit identical helical symmetry in their precontracted state (Hardy et al., 2022). This symmetry is relatively straightforward to identify due to the presence of only two prominent layer lines $n = 0$ and $n = 6$ in its power spectrum. However, during the bacteriophage life cycle, the tail sheath undergoes contraction of up to 25% of its original length, leading to a scenario where the tube and sheath adopt different helical symmetries. While it has been assumed that the tube structure remains unchanged when the surrounding sheath contracts (Leiman and Shneider, 2012), this has never been determined experimentally until very recently (Sonani et al., 2024b), due to the fact that in the post-contracted state there will be a superposition of two different helical symmetries.

Figure 3a shows a cryo-electron micrograph of the post-contracted tail of myophage Milano, infecting the soil bacterium *Agrobacterium tumefaciens* (Nittolo et al., 2019; Sonani et al., 2024b). Figure 3b is the 2D class average of contracted tail segments showing the overlapping projection of tube and sheath having different helical symmetries. Figure 3c shows a simulated top view of the contracted tail, with the tube in violet and the sheath in grey. The size of the sheath protein is nearly four times larger than the tube protein, resulting in a sheath:tube mass ratio
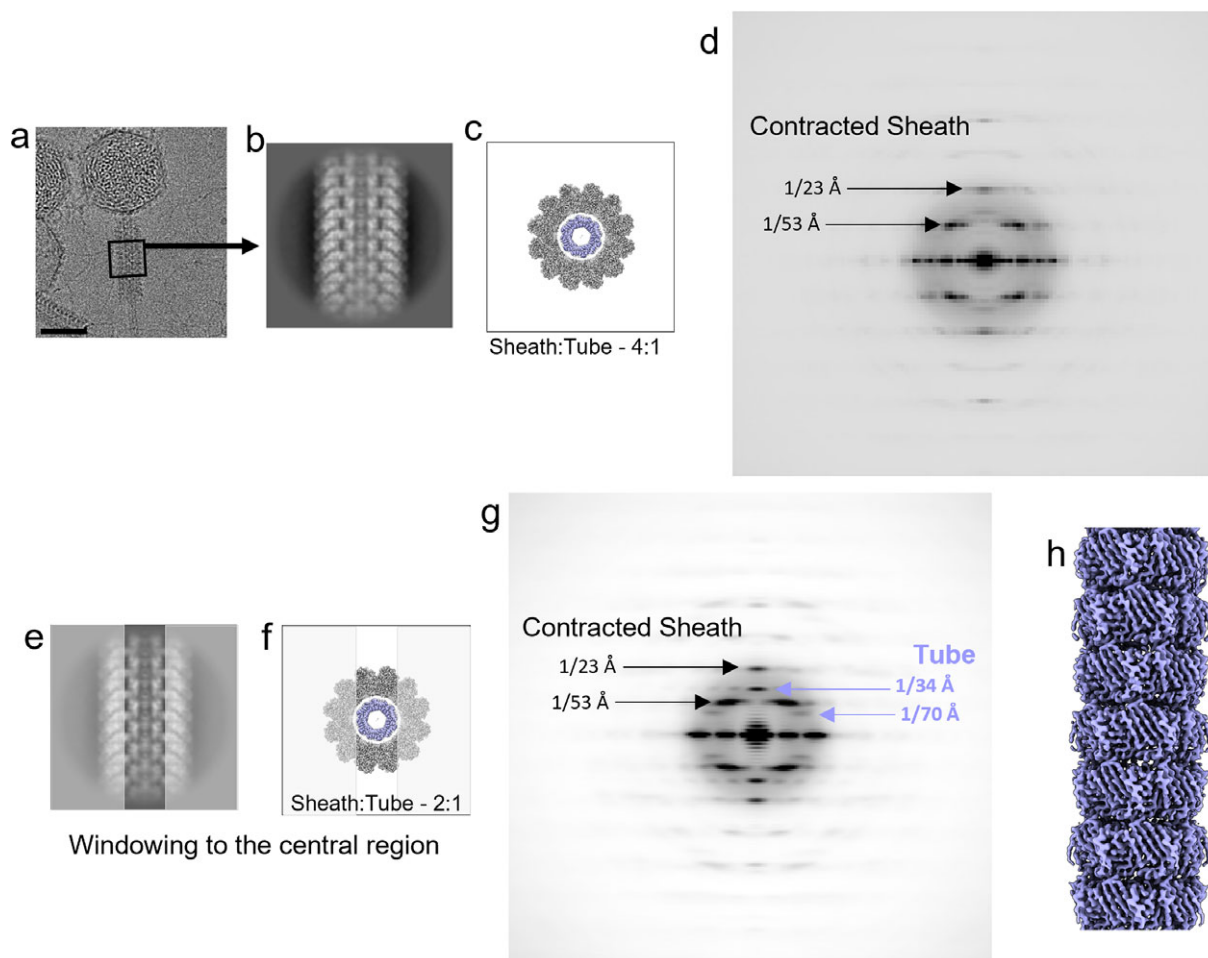
Figure 3. A case with mixed helical symmetries. (a) Cryo-EM micrograph, (b) 2D-class average, (c) simulated top-view, and (d) average power spectrum of segments of postcontracted tail of *Myoviridae* phage Milano. Windowing of the central part of the post-contracted tail to remove the excess signal from contracted sheath is depicted on (e) 2D class average, and (f) simulated top view of postcontracted tail. (g) Average power spectrum of centrally windowed post-contracted tail segments showing the layer lines corresponding to the central tube in addition to the contracted sheath. (h) 3D map (EMD-29354) of post-contracted tube reconstructed using the tube helical parameters. The tail-tube and tail-sheath are shown in violet and grey, respectively, in (c) and (f). (Sonani et al., 2024b).

of ~4:1 in projected images. This causes the sheath signal to completely dominate the weak tube signal. Consequently, the power spectrum (Figure 3d) derived from the contracted tail segments predominantly shows layer lines arising from the sheath. Specifically, the layer lines at ~1/(34 Å) ($n = 0$) and ~ 1/(17 Å) ($n = 6$) are attributed to the sheath symmetry, with no discernible layer lines arising from the tube symmetry. This problem kept the post-contracted tube structure unresolved and speculative for a long time (Fraser et al., 2021; Leiman and Shneider, 2012).

The strategy to solve this problem involved windowing of raw tail segments (Sonani et al., 2024b). As shown in Figure 3e, the tail segments were tightly masked to decrease the signal from the sheath and increase the relative contribution of the tube. As shown in the simulated top view (Figure 3f), this cannot completely eliminate the signal from sheath but reduces the sheath:tube mass ratio to ~2:1. The power spectrum of these windowed segments (Figure 3g) reveals additional layer lines at approximately 23 Å and 12 Å, which correspond to the helical symmetry of the tube. Indexing these layer lines as $n = 0$ and $n = 6$, respectively, yielded helical symmetry parameters of 28.2° twist and 34.0 Å rise. Imposing these parameters made possible a ~ 3.3 Å reconstruction of the tube enclosed within a contracted sheath (Figure 3h) due to the fact that the mass of the surrounding sheath is averaged out because of its different helical symmetry.

Bacterial flagellar filaments with outer domain multimers

Flagella are motility devices that have convergently evolved across the three domains of life (bacteria, archaea and eukaryotes) to allow cells to swim in solution (Beeby et al., 2020). While it has been proposed that the archaeal flagellum should be called an 'archaellum' due to the fact that it has no homology with the bacterial flagellum (Jarrell and Albers, 2012), we have many examples where analogous, but nonhomologous systems in biology retain the same name. Birds, bats, and bees have wings, but these are analogous and do not have a common ancestry. Insects and mammals have legs, but these appendages also have no common ancestry. We and others (Wirth, 2012) have therefore argued that all three should retain their classical description as flagella, even though none of the main components of the three flagellar systems share homology. The eukaryotic cilium is very similar to the eukaryotic flagellum, but the term flagellum is used to describe the undulating tails of motile cells such as sperm and protists, and these tails are not called cilia. For example, a PubMed search for 'sperm' AND 'flagellum' returns 1,517 papers. Similarly, a search for 'trypanosome' AND 'flagellum' returns 182 papers. While the eukaryotic flagellum is composed of hundreds of different components (Pazour et al., 2005), bacterial and archaeal flagellar filaments are much simpler and in general are mainly composed of thousands of copies of a single protein, flagellin. Despite having no homology, bacterial and archaeal flagellins have convergently evolved to assemble into filaments with three-dimensional supercoils using strikingly similar mechanisms (Kreutzberger et al., 2022b). The structures of bacterial flagellar filaments have been studied extensively since the 1970's (Kamiya and Asakura, 1976; Wakabayashi and Mitsui, 1970) with some papers dating back even earlier (Pijper and Abraham, 1954). Until recently, almost all structural studies were done exclusively on nonmotile mutant straight (as opposed to supercoiled) flagellar filaments that were found to contain all left-handed (L-type) or right-handed (R-type) protofilaments (Hyman and Trachtenberg, 1991; Kreutzberger et al., 2020; Maki-Yonekura

et al., 2010; Samatey et al., 2001; Wang et al., 2017; Yonekura et al., 2003). There are 11 protofilaments formed by the protein flagellin in these filaments, and in the L-type and R-type mutants all 11 protofilaments are either left-handed or right-handed, respectively. In these straight mutants, helical symmetry exists such that every flagellin molecule is in an identical environment. More recently, there have been many structures obtained from supercoiled flagellar filaments which retain their curvature in the relatively thin ice of cryo-EM conditions (Blum et al., 2019; Fields et al., 2024; Gibson et al., 2020; Kreutzberger et al., 2022a; Kreutzberger et al., 2022b; Montemayor et al., 2021; Nedeljkovic et al., 2023; Sanchez et al., 2023). However, the majority of these cryo-EM reconstructions still imposed helical symmetry, even though it is not strictly present in the supercoiled state. The proposed mechanistic basis for bacterial flagellar filament supercoiling has a long history going back almost 50 years, based upon assumed mixtures of L- and R-state protofilaments (Calladine, 1975; Calladine et al., 2013; Kamiya et al., 1980; Kamiya et al., 1982). The relevance of the L- and R-type mutants appears to have diminished, as a recent study showed that neither of these two conformations exist in the wildtype supercoiled structures as determined by cryo-EM (Kreutzberger et al., 2022b). Given the long history of flagellar filament structural biology, an entire review on just this subject would be required to do justice to the many papers that have been produced. This is well beyond the scope of the present review, and we will focus on some examples of both the distinct helical symmetries adopted by flagellar filaments, and how this symmetry can be broken by supercoiling.

All flagellar filaments have an overall symmetry that is dependent on the protein domains D0 and D1 found in the inner core of every flagellar filament. If one were to obtain cryo-electron micrographs of flagellar filaments (Figure 4a) and process them to obtain an averaged power spectrum, many types of flagellar filaments would have a power spectrum resembling the one shown in Figure 4b. Two such examples are flagellar filaments from *Bacillus subtilis* (Wang et al., 2017) (Figure 4c) and *Campylobacter jejuni* (Kreutzberger et al., 2020) (Figure 4d). The most prominent layer lines in this power spectrum are from the 1-, 5- and 6-start helices. However, straight L- and R-type flagellar filaments may also produce a power spectrum with a clear $n = 11$ layer line arising from the 11-start helix (Wang et al., 2017). These flagellar filaments have helical symmetry parameters that vary slightly depending on whether the filaments are straight (L-type/R-type) or in different supercoiled states (Normal, Curly I, Curly II, etc.) (Calladine et al., 2013; Wang et al., 2017). For all these symmetries, the helical rise typically varies between about 4.4 Å and 5.0 Å and the twist varies between 65.3° and 65.8°. We will refer to this as a canonical or monomeric flagellar filament symmetry, as the asymmetric unit in the filament contains a single flagellin molecule. Helical symmetries can be easily plotted as helical nets, which is the unrolled surface lattice. In Figure 4e, the helical net of a canonical flagellar filament with a monomeric symmetry is shown.

While the *B. subtilis* and *C. jejuni* flagellar filaments have similar helical symmetries, there are additional domains (called outer domains) in the *C. jejuni* filament. The *B. subtilis* flagellin only has core domains D0 and D1, while the *C. jejuni* flagellin has additional domains D2, D3, and D4. These domains are on the surface of the filament and result in the *C. jejuni* filament having a larger diameter than the *B. subtilis* one. The model system for many earlier structural studies was the *Salmonella typhimurium* flagellar filament, which contains outer domains D2 and D3. However, there is no homology between these *Salmonella* outer domains and the
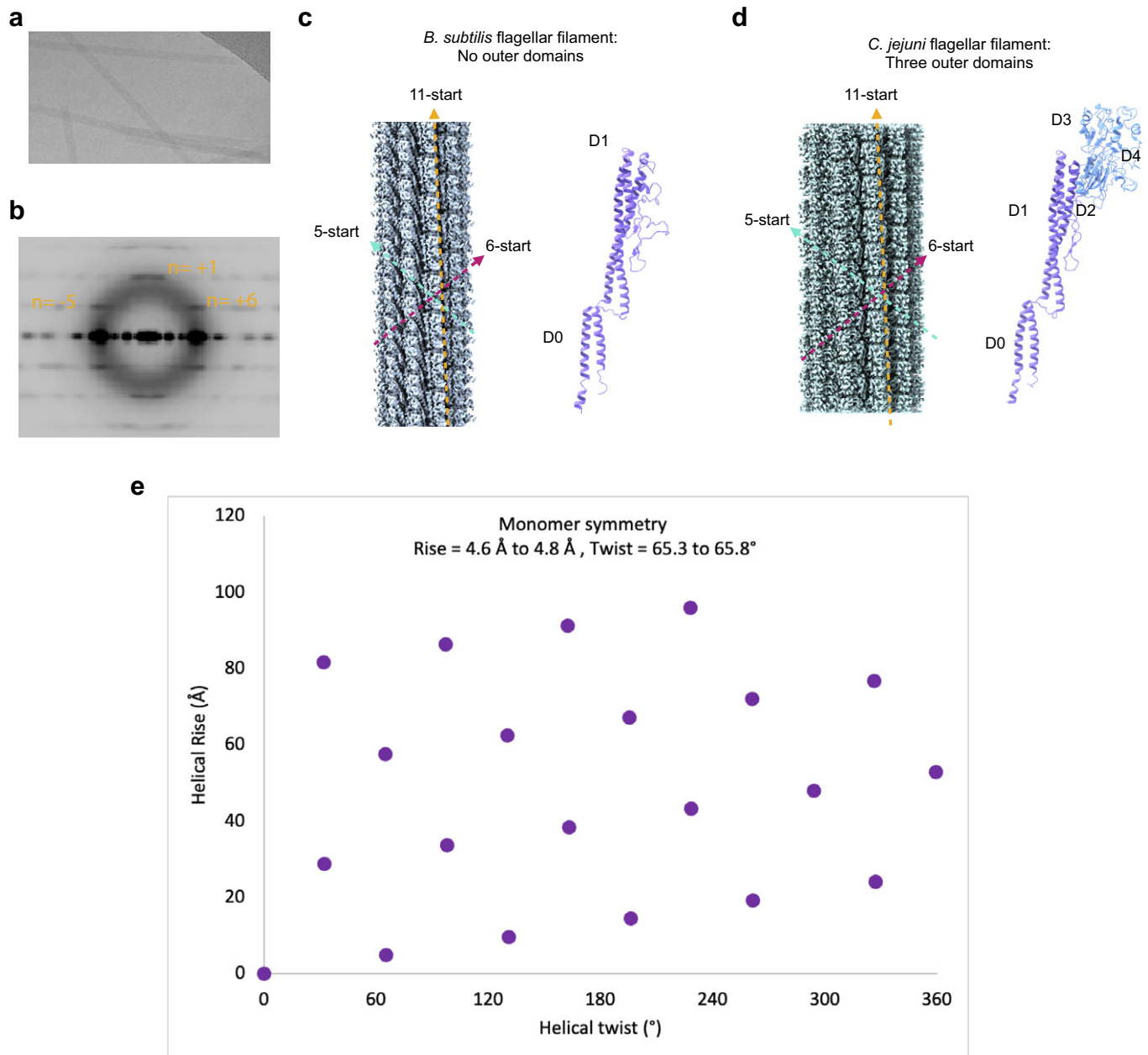
Figure 4. Bacterial flagellar filaments with monomer symmetries. (a) Cryo-electron micrograph of straight mutant flagellar filaments. (b) Averaged power spectrum from flagellar filament segments showing the canonical flagellar filament layer lines. (c) Helical reconstruction of a *B. subtilis* flagellar filament (left) and a single flagellin atomic model (right) built from the density map. (d) Helical reconstruction of the *Campylobacter jejuni* flagellar filament (left) and a *C. jejuni* flagellin atomic model built from the density map (right). (e) Helical net, or surface lattice, represents the canonical flagellar filament symmetry, also called "monomeric symmetry". The symmetry plotted corresponds to a helical rise of 4.8 Å and a twist of 65.4°. Data from Wang et al., 2017 and Kreutzberger et al., 2020.

C. jejuni ones, but they are still given the same name solely to indicate their position in the flagellin fold. In both, the cases of the *C. jejuni* and *S. typhimurium* flagellar filaments, any packing interactions that the outer domains make do not contribute to the symmetry of the filament. We know this because these filaments have the same symmetry as the *B. subtilis* filaments, which have essentially no outer domain (only a very small loop region is present). However, we will show how some flagellin outer domains can drastically alter the overall symmetries of their respective filaments by establishing new packing interactions on the filament surface, although these new contacts do not alter the interactions in domains D0 and D1.

There were numerous early studies which described flagellar filaments with 'perturbed' symmetries (Cohen-Krausz and Trachtenberg, 1998; Kamiya et al., 1982; Trachtenberg et al., 1987; Trachtenberg et al., 1998) due to power spectra with extra layer lines in addition to the typical canonical ones. These additional layer lines indicated that there was a larger asymmetric unit than a single flagellin in these filaments, likely arising from interactions among the outer domains that were altering the symmetry as a whole. Recent studies using cryo-EM have found similar cases where the overall filament symmetry is different from the canonical one (Fields et al., 2024; Kreutzberger et al., 2022a; Wang et al., 2017). In some flagellar filaments, the overall surface of the filament
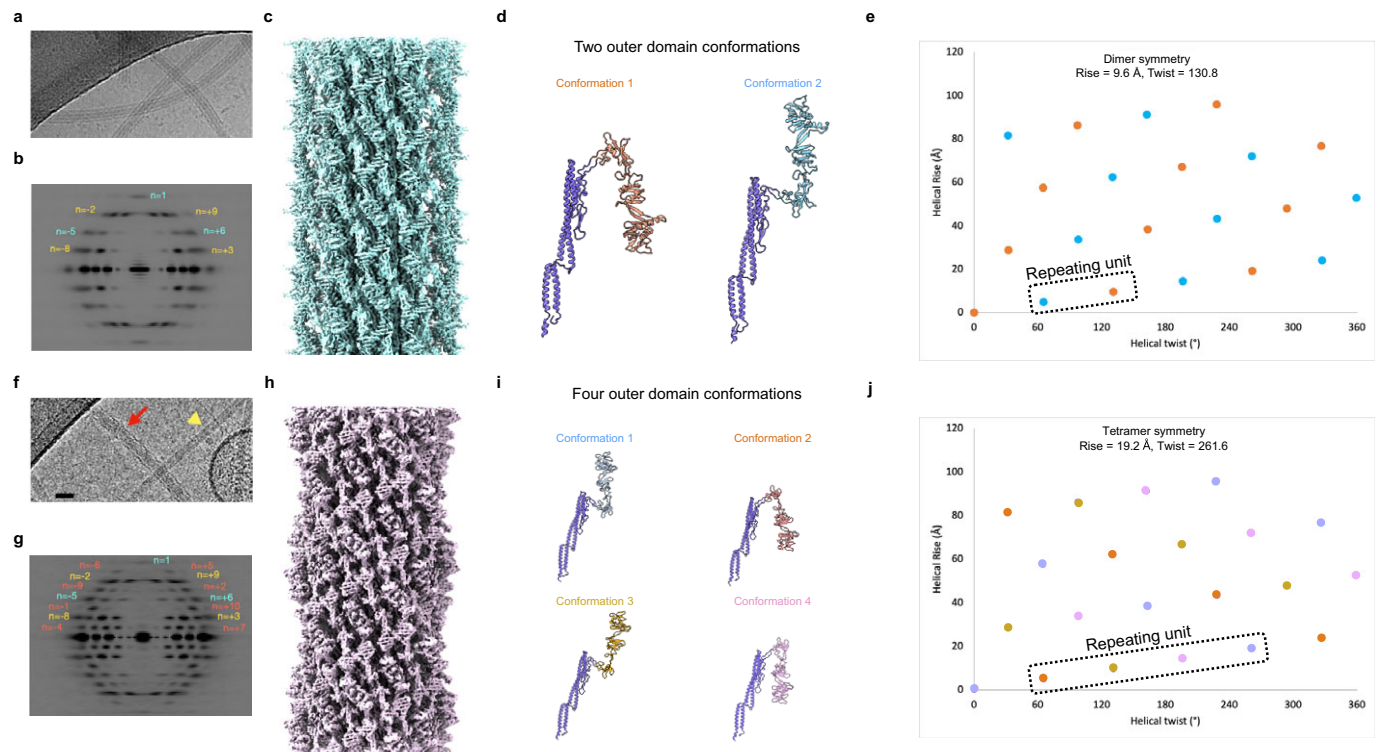
Figure 5. Bacterial flagellar filaments with dimeric and tetrameric symmetries. (a) Cryo-electron micrograph of supercoiled EHEC O157:H7 flagellar filaments. (b) Averaged power spectrum of EHEC H7 flagellar filaments shows twice the number of layer lines present when compared to a canonical flagellar filament. (c) Density map of the EHEC H7 dimer flagellar filament. (d) Atomic models for the two flagellin conformations found in the EHEC O157:H7 flagellar filament. Note that the core D0/D1 domains (purple) are identical, and the outer domains are rotated by 180° between the two conformations. (e) Helical net showing the symmetry of the EHEC H7 flagellar filament. The symmetry is denoted as a 'dimeric symmetry' because the rise and twist are twice that of a canonical monomeric flagellar filament, and the asymmetric unit contains two flagellin molecules. The two outer domain conformations are represented by two different colors. The asymmetric unit is denoted by the dashed box. (f) Cryo-electron micrograph of the *Achromobacter* flagellar filament (red arrow), which appeared as a contaminant in a preparation from *Agrobacterium tumefaciens*. The yellow triangle points to an *A. tumefaciens* flagellar filament. (g) Averaged power spectrum of *Achromobacter* flagellar filament segments. There are four times the number of layer lines present when compared to the canonical flagellar filament. (h) Density map of the *Achromobacter* flagellar filament from helical reconstruction using a tetrameric symmetry (where the asymmetric unit contains four flagellin molecules). (i) Atomic models of the four *Achromobacter* flagellin conformations. Note that the core domains are all identical in these four conformations. There are two 'up' and two 'down' conformations. The two distinct conformations of each 'up' and 'down' orientation differ from each other by the radius at which the outer domain extends from the core. (j) Helical net of the *Achromobacter* flagellar filament. The four flagellin conformations in the tetrameric symmetry are represented by four different colors. The repeating asymmetric unit of four flagellins is indicated by the dashed box. Data from Kreutzberger et al., 2022a.

is noticeably different, and this can be seen in raw electron micrographs such as the one from *E. coli* O157:H7 (EHEC O157:H7) shown in Figure 5a. The averaged power spectrum of multiple segments of EHEC H7 flagellar filaments shows twice the number of layers lines as expected for a canonical flagellar filament (Figure 5b). However, knowing that this is a flagellar filament makes determining the symmetry much easier. Since the $n = +1$, $n = -5$, and $n = +6$ layer lines occur at approximately the same spacings for the EHEC H7 flagellar filament as they do in canonical flagellar filaments, the simplest explanation is that the additional layer lines arise from a larger asymmetric unit. Calculation of the symmetry from the EHE H7 power spectrum shows a helical rise of ~9.6 Å and a helical twist of ~130.8°, values that are roughly double those of the canonical flagellar filament symmetry parameters, showing that the asymmetric unit has doubled.

Helical reconstruction with these parameters results in a density map with unique surface features (Figure 5c) that atomic model building reveals to be the result of the EHEC flagellin outer domains having two distinct conformations that are related to each other by a 180° rotation (Figure 5d). When these two conformations are mapped onto a helical net with a monomeric symmetry, the overall symmetry of the dimer flagellar filament can be clearly visualized (Figure 5e). Such a huge conformational change (a 180° rotation of

half of the outer domains) cannot in any way be considered a 'perturbation', in stark contrast with the earlier descriptions (Trachtenberg et al., 1986). Similarly, a flagellar filament belonging to the genus *Achromobacter* also has unique surface patterns revealed in electron micrographs (Figure 5f), and analysis of their power spectrum revealed four times the number of layer lines when compared to a canonical flagellar filament (Figure 5g). Determination of the helical symmetry from the power spectrum resulted in a tetrameric symmetry with a helical rise of ~19.2 Å and a helical twist of ~261.6°, values that are quadruple those of canonical flagellar filament symmetries. Helical reconstruction using this tetrameric symmetry resulted in a high-resolution density map with unique surface features (Figure 5h) and subsequent model building revealed four unique flagellin outer domain conformation (Figure 5i). Such a tetrameric symmetry can also be visualized on a helical net plotted using the monomeric symmetry, but the asymmetric unit now contains four flagellin molecules (Figure 5j).

Filaments with seams

The notion of breaks or 'seams' in helical symmetry has been present in the field of helical assemblies for quite some time. Perhaps the most well-known example is the seam that occurs in
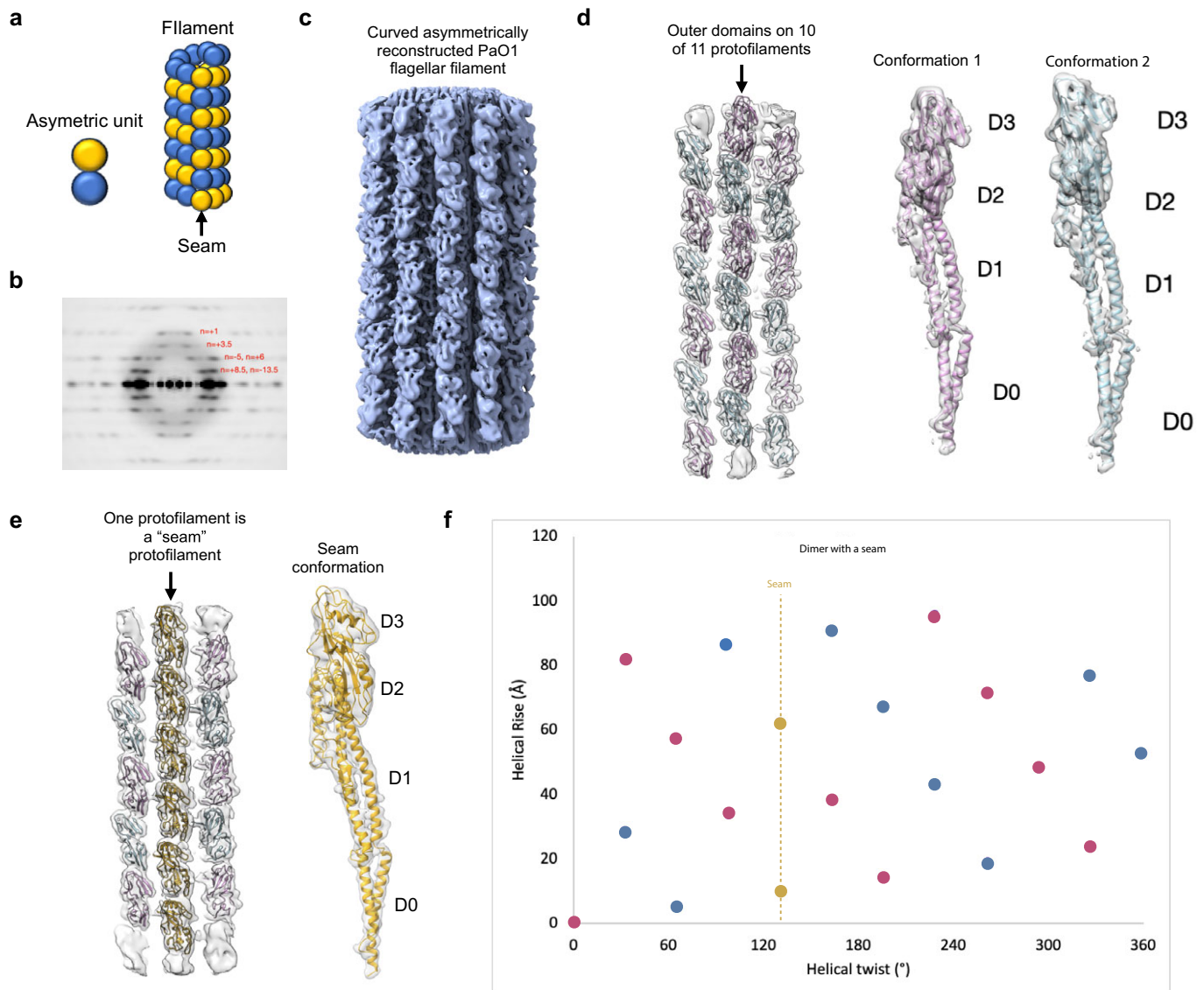
Figure 6. Cryo-EM structure of the *Pseudomonas aeruginosa* PAO1 flagellar filament with a dimer seam. (a) Cartoon explaining the basic concept of a seam in a filamentous assembly. A seam is any break in the symmetry pattern in that filamentous assembly. The cartoon shown here is modeled after the seam found in microtubules. (b) Power spectrum of the PAO1 flagellar filament showing layer lines of non-integer Bessel orders. (c) PAO1 asymmetric density map with curvature present. (d) On the left is the density map and fit of outer domain models of three neighboring PAO1 protofilaments on the surface of the flagellar filament. There are two outer domain conformations indicated by the blue and pink outer domain models. The models for the two flagellin conformations are shown on the right, each fit into their corresponding subunit density. (e) On the left, the surface of the PAO1 flagellar filament map and fit of models is shown where a distinct third conformation (gold) breaks the alternating pattern between conformations 1 and 2. This break in the pattern is called a seam. The right image shows a single PAO1 seam subunit model (gold) fit into its corresponding density map. (f) Helical net depicting the PAO1 outer domain conformations (pink or blue) as well as the third seam conformation (gold). The net was created showing that the core of the filament had a canonical helical symmetry with a rise of 4.8 Å and a twist of 65.4°. Data from Nedeljkovic et al., 2023.

microtubules (Kikkawa et al., 1994). This break in the symmetry of the microtubule lattice is due to a register switch along a line in the filament where the pattern of αβαβ… is broken (Figure 6a). At low resolution, α and β tubulin look identical, and thus, the seam would not be seen. However, microtubule-binding proteins such as kinesin bind to α- and β-tubulin differently, and thus can be used to visualize the seam at low resolution (Kikkawa et al., 1994). Seams arising in bacterial flagellar filaments due to a pairing of subunits have been called 'non-helical perturbations' (Trachtenberg et al., 1998), as opposed to the 'helical perturbations' that arise from a pairing of subunits that leave helical symmetry intact, albeit with double the asymmetric unit. Such an example of a seam in *Pseudomonas aeruginosa* strain PAO1 was reconstructed at low resolution

(Wang et al., 2017). While the PAO1 power spectrum in Figure 6b suggests a dimer symmetry similar to the EPEC H7 filament, further analysis reveals that the additional layer lines contain non-integer Bessel orders, and that the filament cannot have a strict dimeric helical symmetry such as found in the EPEC H7 filaments. Recently, a scheme has been developed to asymmetrically reconstruct bacterial flagellar filaments to reveal features such as curvature and supercoiling (Kreutzberger et al., 2022b). While described in greater detail in the sections below, this same reconstruction methodology was used to solve the PAO1 flagellar filament structure to a reasonable resolution (Figure 6c) (Nedeljkovic et al., 2023). Model building and analysis revealed that 10 out of the 11 PAO1 protofilaments had a repeating pattern where the outer domains of

each flagellin on the same protofilament alternated between two conformations (Figure 6d). However, one protofilament did not have such a pattern and formed the seam where all subunits on this protofilament had the same outer domain conformation (Figure 6e). Such a seam can also be easily visualized using a helical net where each point corresponds to a flagellin with the monomeric symmetry, but the respective outer domain conformations are indicated by the points having three different colors (Figure 6f).

Subunit multimerization in extracellular archaeal filaments

As previously noted, bacterial and archaeal flagellar filaments share no structural homology. In fact, archaeal flagella are structural homologues of bacterial and archaeal type 4 pili (T4P) (Faguy et al., 1994). All archaeal flagellar filaments that have been studied have a symmetry with a rise of ~5.3 Å and a twist of ~108° (Kreutzberger et al., 2023). Archaeal flagellin consists of an N-terminal α-helical domain and a C-terminal largely β-sheet globular domain (Figure Mark 4a). The C-terminal globular domains can

vary quite a bit in size, while the N-terminal helices are all around 45 amino acids in length (give or take a few residues depending on the species) (Kreutzberger et al., 2023). This flagellin domain organization is shown for the *Methanospirillum hungatei* archaeal flagellar filament (Poweleit et al., 2016) in Figure 7a. The power spectrum for the *M. hungtai* filament is shown in Figure 7b. Strikingly similar in concept to the multimerization of bacterial flagellin outer domains, the recent *Methanocaldococcus villosus* archaeal flagellar filament structure (Gambelli et al., 2022) revealed a filament composed of two different flagellins arranged into an asymmetric unit of 6 flagellins Figure 7c, containing three copies each of flagellins ArlB1 and ArlB2. While this hexameric flagellar filament has a striking packing pattern (Figure 7c), the differences between this hexameric filament's power spectrum (Figure 7d) and a monomeric one (Figure 7b) are quite subtle compared to the differences observed for bacterial flagellar filaments. The most noticeable difference between the monomeric *M. hungtai* power spectrum (Figure 7b) and the hexameric one is the presence of a n = 0 layer line found at ~1/(33 Å) in the *M. villosus* power spectrum (Figure 7d). While the *M. villosus*

a. Monomeric symmetry archaeal flagellar filament (*M. hungtai*)

C-terminal globular domain

Side view

N-terminal helix

Top view

b.

n=0 at1/5.3 Å

c. Hexameric symmetry archaeal flagellar filament (*M. villosus*)

ArlB1

ArlB2

Side view

6 subunit ASU

d.

n=0 at1/33.4 Å
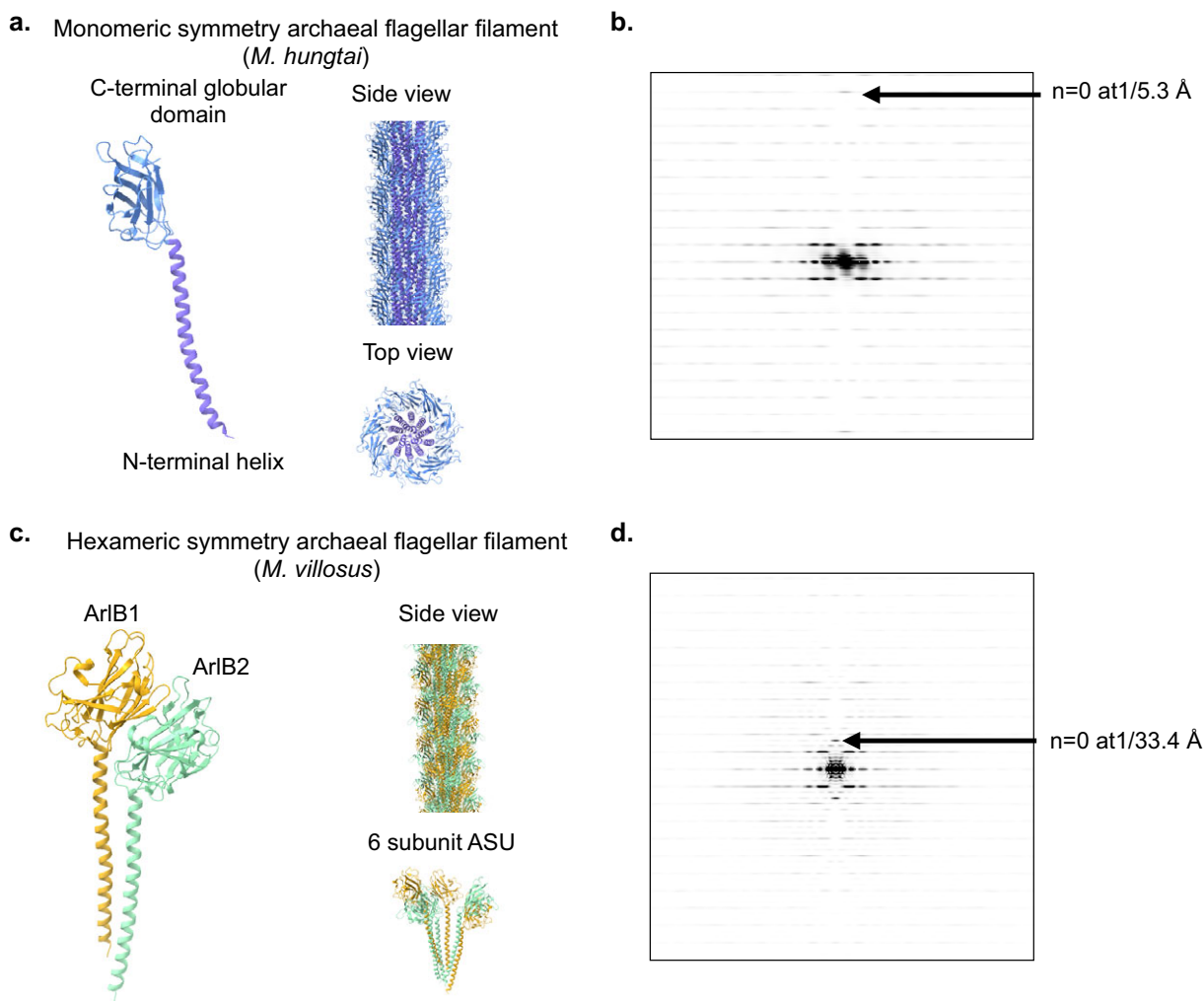
Figure 7. Archaeal flagellar filaments with monomeric and hexameric symmetries (a) The image on the left shows a single *M. hungtai* archaeal flagellin. The images on the right show the *M. hungtai* archaeal flagellar filaments from side and top views. (b) Power spectrum generated from the *M. hungtai* filament model. (c) The image on the left shows the two *M. villosus* archaeal flagellins, ArlB1 and ArlB2. The right top image shows the *M. villosus* filament colored according to its two distinct flagellins. The image on the right bottom shows the asymmetrical unit of the *M. villosus* filament consisting of six flagellins (three copies of ArlB1 and three copies of ArlB2). (d) Power spectrum generated from a model of the *M. villosus* archaeal flagellar filament. The helical model was created by taking the asymmetrical unit containing six flagellins and imposing helical symmetry on them in ChimeraX (Meng et al., 2023).

archaeal flagellar filament contains an asymmetric unit of multiple subunits, it is unique from currently known bacterial flagellar filament structures because its asymmetric unit contains two distinct proteins rather than one protein that adopts multiple conformations. More recently, two different studies have identified archaeal type IV pili, where the asymmetric unit consists of three identical copies of a type IV pilin that adopts three distinct outer domain conformations (Gaines et al., 2024; Liu et al., 2024). Strikingly, in one study, the same pilin was found to also form a type IV pilus where it only adopted a single conformation (Liu et al., 2024).

Asymmetric reconstruction of filamentous assemblies with pseudo-helical symmetry

While symmetry is ubiquitous in nature, deviations from perfect symmetry often exist. For instance, icosahedral virus capsids often display asymmetry in various regions (Jose and Hafenstein, 2022). Although an icosahedral symmetric reconstruction technique can achieve markedly higher resolution, it loses crucial asymmetric details, which are often biologically significant. Recent advancements in cryo-EM have greatly enabled asymmetric reconstructions, thereby providing valuable new biological insights into viral structures (DiNunno et al., 2020; Goetschius et al., 2021; Liu et al., 2019).

Similarly, helical polymers exhibit clear deviations from helical symmetry such as bending. Generally, such deviations can be ignored in the single particle approach to helical reconstruction by the use of short segments that are all relatively straight. This approach provides a piece-wise linear approximation to the continuum, so a curved filament can be treated as an ensemble of straight segments if the radius of curvature is large enough. However, curved filaments may instead be treated asymmetrically when the radius of curvature is much smaller. Some examples of polymers that have been reconstructed asymmetrically resulting in high-resolution structures include F-actin (Carl et al., 2024; Reynolds et al., 2022) shown in Figure 8a,b as well as the supercoiled flagellar
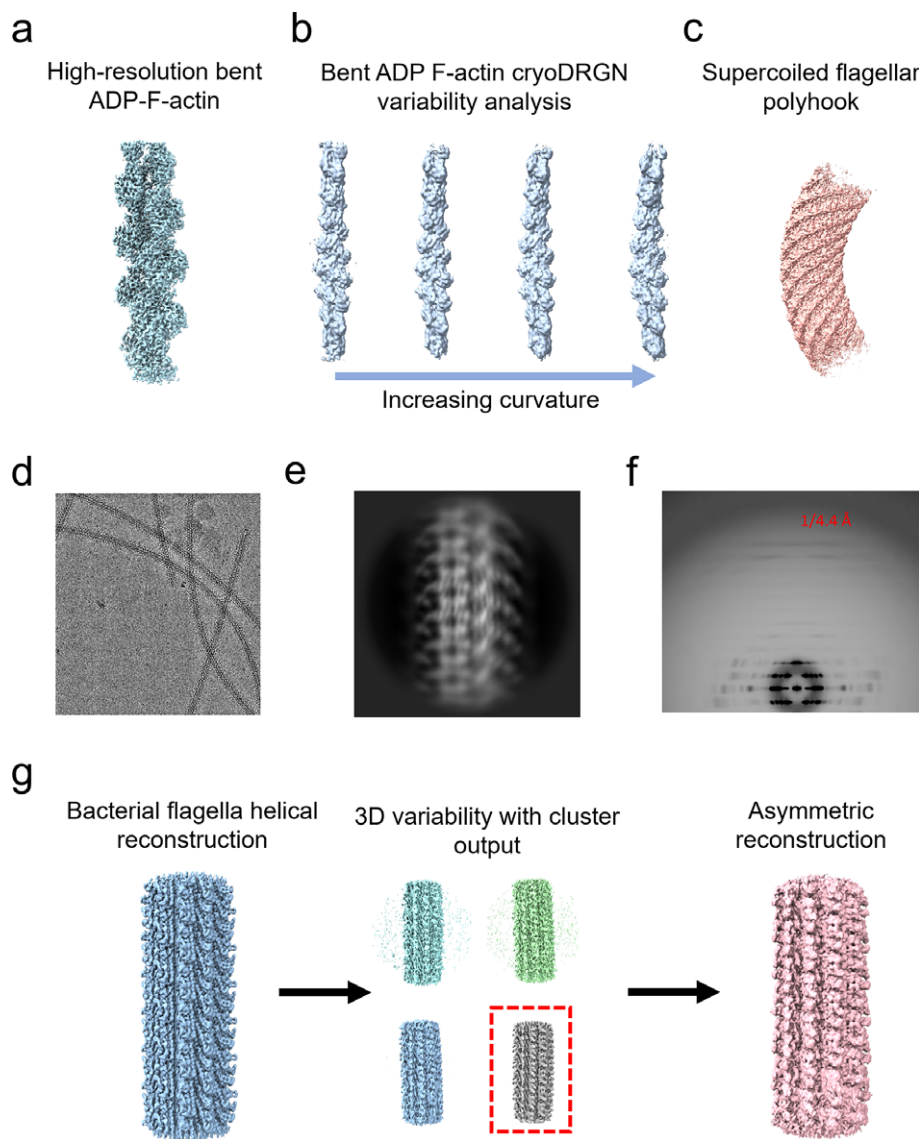
Figure 8. (a) Reconstruction of curved ADP-F-actin. (b) CryoDRGN variability analysis showing the various states of bending in ADP F-actin cryo-EM dataset. (c) Asymmetric reconstruction of a supercoiled flagellar polyhook. (d) Cryo-EM micrograph, (e) 2D-class average, and (f) averaged power spectrum of a supercoiled *E. coli* K12 flagellar filament. (g) Asymmetric reconstruction scheme for a supercoiled flagellar filament. The red dashed box indicates the good cluster which was chosen for subsequent asymmetric reconstruction. Data from Reynolds et al., 2022, Shibata et al., 2019 and Kreutzberger et al., 2022b.

polyhooks as shown in Figure 8c (Kato et al., 2019; Shibata et al., 2019). In the examples described in the previous section, many of the bacterial and archaeal flagellar filaments' high-resolution cryo-EM structures were solved by imposing helical symmetry on filamentous assemblies that were supercoiled and thus did not have true helical symmetry. Supercoiling means that all subunits are not in an identical environment, with some being on the inside of a curve and others being on the outside.

Consider the supercoiled flagellar filaments from *Escherichia coli* K12. Cryo-EM images of these filaments show pronounced bending indicative of supercoiling (Figure 8d) (Kreutzberger et al., 2022b). The 2D class average of 415 × 415 Å segments of these filaments shows nearly undetectable bending at this scale, as shown in Figure 8e. The average power spectrum from these raw segments, shown in Figure 8f, features layer lines extending to high resolution (~4.4 Å), suggesting the presence of a high degree of order. This indicates that the supercoiled flagellar filament can still be reconstructed helically using this smaller box size. Figure 8g shows such a helical reconstruction of a bacterial flagellar filament featuring well-resolved secondary structures. However, all information about supercoiling is lost in this approach as the imposition of helical symmetry eliminates the ability to resolve small conformational differences between subunits, such as those on the inside and outside of the curve. To address this, an asymmetric reconstruction approach can be employed to preserve supercoiling information, as described by Kreutzberger et al. (Kreutzberger et al., 2022b). Using this asymmetric approach cryo-EM maps and models of supercoiled bacterial and archaeal flagellar filaments can be obtained (Figure 8g).

Since the reconstructions of curved filaments are essentially a single-particle cryo-EM reconstruction problem, a variety of different methodologies have been used to provide a suitable starting volume for asymmetric reconstructions. Shibata *et al.* achieved the best results on their flagellar polyhooks structure when starting with a computationally generated supercoiled volume (Shibata et al., 2019). For the reconstructions of bent F-actin, Reynolds *et al.* used a neural network-based approach to select high curvature actin filaments and then generated a starting volume via *ab initio* reconstruction (Reynolds et al., 2022). The continuum of actin curvature states was then characterized using cryoDRGN variability analysis (Zhong et al., 2021). The bacterial flagellar filament *ab initio* reconstructions, in general, yielded poor results (Kreutzberger et al., 2022b). Therefore, several different approaches were taken to yield a curved filament structure, and one approach is shown in Figure 8g. Here, a mask from the helical reconstruction job as well as the individual particles can be used as inputs into a cryoSPARC 3D variability job (Punjani and Fleet, 2021; Punjani et al., 2017; Punjani et al., 2020). If curvature is present in the particles, as is the case for supercoiled bacterial flagella, then the program can be used to generate a curved volume. As with cryoDRGN, cryoSPARC should be able to sort out different curvature states within the same dataset.

Similarly, there are instances where extreme flexibility impedes helical reconstruction. Consider the example of the *Vibrio cholerae* toxin-coregulated pilus (TCP), which appears very flexible by cryo-EM (Figure. 9a) (Sonani et al., 2023). This flexibility is apparent in the 2D class average generated from the 212 × 212 Å size segments (Figure 9b). The average power spectrum (Figure 9c) from these segments shows layer lines extending only up to ~21 Å, reflecting a lack of long-range order. Consequently, the helical reconstruction was limited to ~6 Å resolution (Figure 9d). In such cases, asymmetric reconstruction can be beneficial (Sonani et al., 2023). This method involves identifying subsets of segments with homogeneous bending through extensive 2D and 3D classifications, which can then be used for asymmetric reconstruction with an initial low-resolution 3D map and mask generated by the helical reconstruction. A higher resolution (~3.7 Å) map of the *V. cholerae* TCP was thus achieved by not imposing helical symmetry (Figure 9e). This is almost counter-intuitive, as traditionally, the assumption has been that dropping symmetry will lead to a lower resolution. Similarly, the high-resolution structure of the very flexible *S. sanguinis* type IV pilus was successfully solved by asymmetric reconstruction (Anger et al., 2023).
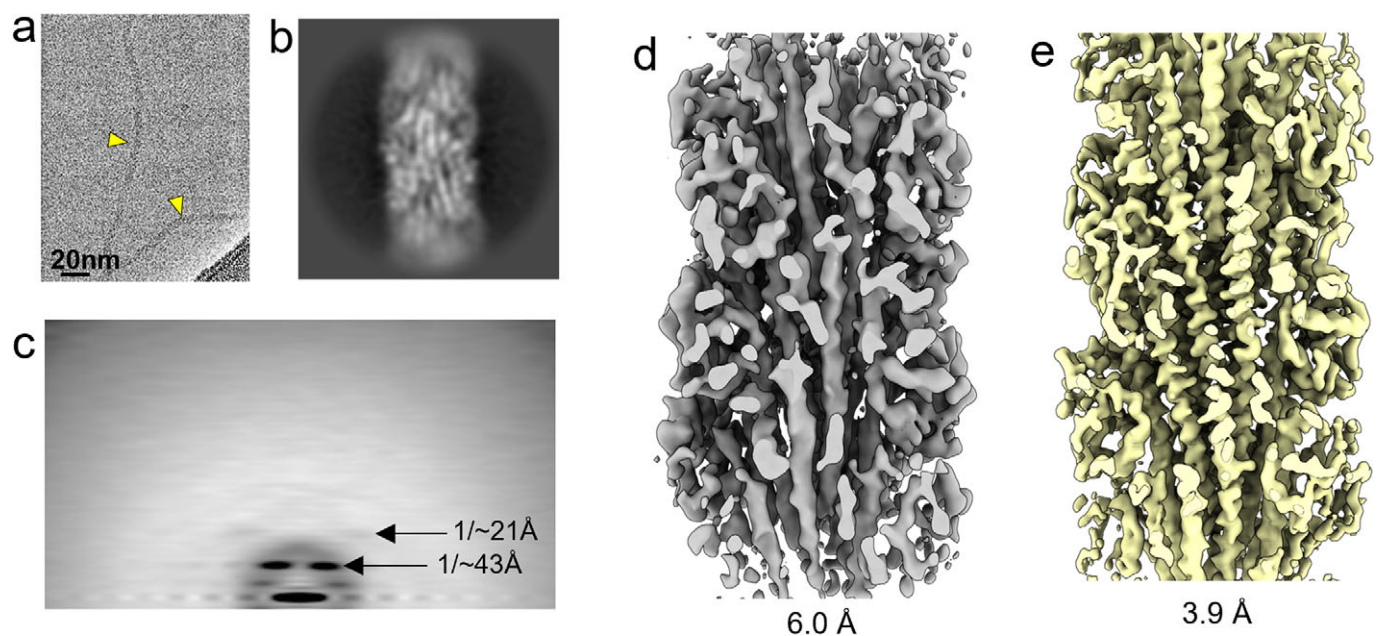

Figure 9. Asymmetric reconstruction of flexible *Vibrio cholerae* toxin-coregulated pilus (TCP). (a) Cryo-EM micrograph, (b) 2D-class average, (c) average power spectrum, (d) helically reconstructed cryo-EM map, and (e) asymmetrically reconstructed cryo-EM map (EMD-42279) of *V. cholerae* toxin coregulated pilus (Sonani et al., 2023).

Conclusion

Advances in software (Nakane et al., 2020; Punjani and Fleet, 2021; Punjani et al., 2020; Schwab et al., 2024; Zhong et al., 2021) and hardware (Sun et al., 2021; Weis and Hagen, 2020) continue to drive the 'revolution' in resolution that has transformed the field of cryo-EM. Better microscopes, better cameras, and better programs have meant that we can do things today that would have been considered impossible only 5 years ago. One of these things involves completely dropping helical symmetry, which can give new insights into everything from actomyosin force generation (Carl et al., 2024) to the supercoiling of prokaryotic flagellar filaments (Kreutzberger et al., 2022b).

While the simplest examples of helical symmetry in biology involve identical subunits being in identical environments in a filament or tube, we have provided many examples where this clearly is not the case, such as where the same subunit can exist in two, three, or four different conformations within the same polymer (Gaines et al., 2024; Kreutzberger et al., 2022a; Liu et al., 2024). The supercoiling of flagellar filaments, necessary for motility since the rotation of a straight filament does not generate thrust, arises from identical subunits adopting multiple conformations. While early models for bacterial flagellar supercoiling were based upon the notion that there were two discrete conformational states in the flagellar filament, more recent results show that this is not the case, and there can be 11 different states (Kreutzberger et al., 2022b). An earlier study of the bacterial flagellar hook actually visualized 11 different states within that assembly (Shibata et al., 2019), providing a tantalizing suggestion that the same might be possible for the flagellar filament.

In the case of the bacterial flagellar filament, the 11 subunit conformations are so similar to each other that the imposition of helical symmetry can still result in a high-resolution structures. The same cannot be said for subunits in the flexible, but not supercoiled, TCP pilus. While never attempted, it is almost certain that helical reconstruction of the supercoiled flagellar polyhooks would have yielded a far inferior structure due to the great degree of curvature present in the reconstruction. Indeed, to achieve the best structure possible with their data, Shibata *et al.* had to create a featureless supercoiled starting volume as *ab initio* reconstructions yielded artifacts. As technology continues to improve in the field, creative solutions to cryo-EM structural determination will become simpler, and structures that are currently thought of as impossible to solve will become solvable.

We have not discussed the role of cryo-electron tomography (cryo-ET) in determining the structure of helical polymers (Bharat et al., 2012; Zhang and Mahamid, 2024). As the resolution of cryo-ET continues to improve (Hutchings and Villa, 2024; Noble and de Marco, 2024), it is certainly reasonable to expect that the structure of an increasing number of helical assemblies will be solved *in situ*, as opposed to current practice using purified samples. Such an approach has already been applied to muscle fibers, with great success (Tamborrini et al., 2023).

In some cases, these newer methodological advances for helical structure determination should perhaps be thought of as an expansion of the tools available to structural biologists rather than strictly replacing the older methods. While software packages such as Relion and cryoSPARC can lead to quick and efficient structural determination of many helical filaments, not every structure is simple. In fact, in one of the examples above (Figure 2), the legacy software package Spider (Frank et al., 1996) proved to be more effective in initial structural determination than these more modern packages. Thus, it is important to consider that sometimes older, legacy software can still be useful.

As with many areas of science, we expect that advances in machine learning and artificial intelligence will play a large role in expediting the analysis of helical polymers in the future (Egelman, 2024). As we discussed here, we currently do not have useful metrics that can distinguish correct from incorrect symmetries. The determination of the correct symmetry is usually made because it is the only one that generates all the features that we expect from proteins, such as secondary structure and side chains. However given the huge and growing database of protein maps, machines can be trained to recognize which ones are correct and which are artifacts. So, it is reasonable to expect that the experience currently needed to recognize a correct map from an incorrect one will be replaced in the future by intelligent programs.

Key Terms. **Power spectrum**: The intensities (the amplitudes squared) in a Fourier transform. This discards the phase information as the Fourier transform contains both amplitudes and phases. Since phases are discarded power spectra from different filament segments can be simply added together without the need for alignment. In other words, the power spectrum from a single filament is invariant under translations of the filament.
Equator: A line in the Fourier transform (FT) or power spectrum of a helical filament that is perpendicular to the filament axis and passes through the origin (the center of the FT). This line corresponds to the Fourier transform of the filament density when projected perpendicular to the filament axis, and is related to the radial density distribution in the filament.
Meridian: A line in the Fourier transform or power spectrum of a helical filament that is parallel to the filament axis and passes through the origin. This line corresponds to the Fourier transform of the filament density when projected onto a line parallel to the filament axis. The lowest resolution intensity on this line typically corresponds to the reciprocal of the rise per subunit.
Bessel function: These are solutions of a differential equation where n is the order of the Bessel function. For integer n (which is the case here, except when seams appear in a structure), these functions are called the cylindrical harmonics because they appear in the solution to Laplace's equation in cylindrical coordinates. It was recognized in the 1950s that the Fourier transform of a helix can be decomposed very simply into Bessel functions of different orders n.
Layer line: Due to axial periodicities in a helical filament, diffraction from these filaments only occurs on discrete lines, called layer lines. In the simplest case, each layer line contains a single Bessel function of order n.

References

Alushin GM, **Lander GC**, **Kellogg EH**, **Zhang R**, **Baker D and Nogales E** (2014) High-resolution microtubule structures reveal the structural transitions in alphabeta-tubulin upon GTP hydrolysis. *Cell* **157**, 1117–1129.

Anger R, **Pieulle L**, **Shahin M**, **Valette O**, **Le Guenno H**, **Kosta A**, **Pelicic V and Fronzes R** (2023) Structure of a heteropolymeric type 4 pilus from a monoderm bacterium. *Nature Communications* **14**, 7143.

Beeby M, **Ferreira JL**, **Tripp P**, **Albers S-V and Mitchell DR** (2020) Propulsive nanomachines: The convergent evolution of archaella, flagella and cilia. *FEMS Microbiology Reviews* **44**, 253–304.

Bharat TA, **Noda T**, **Riches JD**, **Kraehling V**, **Kolesnikova L**, **Becker S**, **Kawaoka Y and Briggs JA** (2012) Structural dissection of Ebola virus and its assembly determinants using cryo-electron tomography. *Proceedings of the National Academy of Sciences* USA **109**, 4275–4280.

Blum TB, **Filippidou S**, **Fatton M**, **Junier P and Abrahams JP** (2019) The wild-type flagellar filament of the Firmicute Kurthia at 2.8 Å resolution in vivo. *Scientific Reports* **9**, 14948.

Calladine CR (1975) Construction of bacterial flagella. *Nature* **255**, 121–124.

Calladine CR, **Luisi BF and Pratap JV** (2013) A "mechanistic" explanation of the multiple helical forms adopted by bacterial flagellar filaments. *Journal of Molecular Biology* **425**, 914–928.

Carl AG, **Reynolds MJ**, **Gurel PS**, **Phua DYZ**, **Sun X**, **Mei L**, **Hamilton K**, **Takagi Y**, **Noble AJ**, **Sellers JR and Alushin GM** (2024) Myosin forces elicit an F-actin structural landscape that mediates mechanosensitive protein recognition. *BiorXiv*, 2024.2008.2015.608188.

Cheng Y, **Han J**, **Song M**, **Zhang S and Cao Q** (2023) Serine peptidase Vpr forms enzymatically active fibrils outside Bacillus bacteria revealed by cryo-EM. *Nature Communications* **14**, 7503.

Cochran WC, **F.H. C.; Vand, V.** (1951) The structure of synthetic polypeptides. I. The transform of atoms on a helix. *Acta Crystallographica* **5**, 581–586.

Cohen-Krausz S and Trachtenberg S (1998) Helical perturbations of the flagellar filament: *Rhizobium lupini* H13-3 at 13 Å resolution. *Journal of Structural Biology* **122**, 267–282.

Crick FH and Watson JD (1956) Structure of small viruses. *Nature* **177**, 473–475.

DeRosier DJ and Klug A (1968) Reconstruction of three-dimensional structures from electron micrographs. *Nature* **217**, 130–134.

Desfosses A, **Ciuffa R**, **Gutsche I and Sachse C** (2014) SPRING - an image processing package for single-particle based helical reconstruction from electron cryomicrographs. *Journal of Structural Biology* **185**, 15–26.

DiNunno NM, **Goetschius DJ**, **Narayanan A**, **Majowicz SA**, **Moustafa I**, **Bator CM**, **Hafenstein SL and Jose J** (2020) Identification of a pocket factor that is critical to Zika virus assembly. *Nature Communications* **11**, 4953.

Egelman EH (2000) A robust algorithm for the reconstruction of helical filaments using single-particle methods. *Ultramicroscopy* **85**, 225–234.

Egelman EH (2007) The iterative helical real space reconstruction method: Surmounting the problems posed by real polymers. *Journal of Structural Biology* **157**, 83–94.

Egelman EH (2010) Reconstruction of helical filaments and tubes. *Methods in Enzymology* **482**, 167–183.

Egelman EH (2014) Ambiguities in helical reconstruction. *eLife* **3**, e04969.

Egelman EH (2024) Helical reconstruction, again. *Current Opinion in Structural Biology* **85**, 102788.

Faguy DM, **Jarrell KF**, **Kuzio J and Kalmokoff ML** (1994) Molecular analysis of archael flagellins: similarity to the type IV pilin-transport superfamily widespread in bacteria. *Canadian Journal of Microbiology* **40**, 67–71.

Fields JL, **Zhang H**, **Bellis NF**, **Petersen HA**, **Halder SK**, **Rich-New ST**, **Wu H and Wang F** (2024) Structural diversity and clustering of bacterial flagellar outer domains. *BioRxiv*.

Frank J, **Radermacher M**, **Penczek P**, **Zhu J**, **Li Y**, **Ladjadj M and Leith A** (1996) SPIDER and WEB: Processing and visualization of images in 3D electron microscopy and related fields. *Journal of Structural Biology* **116**, 190–199.

Fraser A, **Prokhorov NS**, **Jiao F**, **Pettitt BM**, **Scheuring S and Leiman PG** (2021) Quantitative description of a contractile macromolecular machine. *Science Advances* **7**, eabf9601.

Fujii T, **Iwane AH**, **Yanagida T and Namba K** (2010) Direct visualization of secondary structures of F-actin by electron cryomicroscopy. *Nature* **467**, 724–728.

Gaines MC, **Sivabalasarma S**, **Isupov MN**, **Haque RU**, **McLaren M**, **Hanus C**, **Gold VAM**, **Albers SV and Daum B** (2024) CryoEM reveals the structure of an archaeal pilus involved in twitching motility. *Nature Communications* **15**, 5050.

Gambelli L, **Isupov MN**, **Conners R**, **McLaren M**, **Bellack A**, **Gold V**, **Rachel R and Daum B** (2022) An archaellum filament composed of two alternating subunits. *Nature Communications* **13**, 710.

Garcia-Pardo J and Ventura S (2024) Cryo-EM structures of functional and pathological amyloid ribonucleoprotein assemblies. *Trends in Biochemical Sciences* **49**, 119–133.

Gibson KH, **Trajtenberg F**, **Wunder EA**, **Brady MR**, **San Martin F**, **Mechaly A**, **Shang Z**, **Liu J**, **Picardeau M**, **Ko A**, **Buschiazzo A and Sindelar CV** (2020) An asymmetric sheath controls flagellar supercoiling and motility in the leptospira spirochete. *eLife* **9**, e53672.

Goetschius DJ, **Hartmann SR**, **Organtini LJ**, **Callaway H**, **Huang K**, **Bator CM**, **Ashley RE**, **Makhov AM**, **Conway JF**, **Parrish CR and Hafenstein SL** (2021) High-resolution asymmetric structure of a Fab-virus complex reveals

overlap with the receptor binding site. *Proceedings of the National Academy of Sciences USA* **118**, e2025452118.

Hardy JM, **Dunstan RA**, **Lithgow T and Coulibaly F** (2022) Tall tails: Cryo-electron microscopy of phage tail DNA ejection conduits. *Biochemical Society Transactions* **50**, 459–422W.

Hutchings J and Villa E (2024) Expanding insights from in situ cryo-EM. *Current Opinion in Structural Biology* **88**, 102885.

Hvorecny KL and Kollman JM (2023) Greater than the sum of parts: Mechanisms of metabolic regulation by enzyme filaments. *Current Opinion in Structural Biology* **79**, 102530.

Hyman HC and Trachtenberg S (1991) Point mutations that lock Salmonella typhimurium flagellar filaments in the straight right-handed and left-handed forms and their relation to filament superhelicity. *Journal of Molecular Biology* **220**, 79–88.

Jarrell KF and Albers SV (2012) The archaellum: an old motility structure with a new name. *Trends in Microbiology* **20**, 307–312.

Jose J and Hafenstein SL (2022) Asymmetry in icosahedral viruses. *Current Opinion in Virology* **54**, 101230.

Kamiya R and Asakura S (1976) Helical transformations of *Salmonella flagella* in vitro. *Journal of Molecular Biology* **106**, 167–186.

Kamiya R, **Asakura S and Yamaguchi S** (1980) Formation of helical filaments by copolymerization of two types of 'straight' flagellins. *Nature* **286**, 628–630.

Kamiya R, **Hotani H and Asakura S** (1982) Polymorphic transition in bacterial flagella. *Symposia of the Society for Experimental Biology* **35**, 53–76.

Kato T, **Makino F**, **Miyata T**, **Horvath P and Namba K** (2019) Structure of the native supercoiled flagellar hook as a universal joint. *Nature Communications* **10**, 5295.

Kikkawa M, **Ishikawa T**, **Nakata T**, **Wakabayashi T and Hirokawa N** (1994) Direct visualization of the microtubule lattice seam both in vitro and in vivo. *Journal of Cell Biology* **127**, 1965–1971.

Kleinschmidt AK, **Moss J and Lane MD** (1969) Acetyl coenzyme A carboxylase: Filamentous nature of the animal enzymes. *Science* **166**, 1276–1278.

Klug A, **Crick FH and Wyckoff HW** (1958) Diffraction by helical structures. *Acta Crystallographica* **11**, 199–213.

Kreutzberger MAB, **Cvirkaite-Krupovic V**, **Liu Y**, **Baquero DP**, **Liu J**, **Sonani RR**, **Calladine CR**, **Wang F**, **Krupovic M and Egelman EH** (2023) The evolution of archaeal flagellar filaments. *Proceedings of the National Academy of Sciences USA* **120**, e2304256120.

Kreutzberger MAB, **Ewing C**, **Poly F**, **Wang F and Egelman EH** (2020) Atomic structure of the *Campylobacter jejuni* flagellar filament reveals how epsilon proteobacteria escaped toll-like receptor 5 surveillance. *Proceedings of the National Academy of Sciences USA* **117**, 16985–16991.

Kreutzberger MAB, **Sobe RC**, **Sauder AB**, **Chatterjee S**, **Pena A**, **Wang F**, **Giron JA**, **Kiessling V**, **Costa TRD**, **Conticello VP**, **Frankel G**, **Kendall MM**, **Scharf BE and Egelman EH** (2022a) Flagellin outer domain dimerization modulates motility in pathogenic and soil bacteria from viscous environments. *Nature Communications* **13**, 1422.

Kreutzberger MAB, **Sonani RR**, **Liu J**, **Chatterjee S**, **Wang F**, **Sebastian AL**, **Biswas P**, **Ewing C**, **Zheng W**, **Poly F**, **Frankel G**, **Luisi BF**, **Calladine CR**, **Krupovic M**, **Scharf BE and Egelman EH** (2022b) Convergent evolution in the supercoiling of prokaryotic flagellar filaments. *Cell* **185**, 3487–3500.

Kuhlbrandt W (2014) Biochemistry. The resolution revolution. *Science* **343**, 1443–1444.

Leiman PG and Shneider MM (2012) Contractile tail machines of bacteriophages. *Advances in Experimental Medicine and Biology* **726**, 93–114.

Liu J, **Eastep GN**, **Cvirkaite-Krupovic V**, **Rich-New ST**, **Kreutzberger MAB**, **Egelman EH**, **Krupovic M and Wang F** (2024) Two distinct archaeal type IV pili structures formed by proteins with identical sequence. *Nature Communications* **15**, 5049.

Liu Y-T, **Jih J**, **Dai X**, **Bi G-Q and Zhou ZH** (2019) Cryo-EM structures of herpes simplex virus type 1 portal vertex and packaged genome. *Nature* **570**, 257–261.

Lovestam S and Scheres SHW (2022) High-throughput cryo-EM structure determination of amyloids. *Faraday Discussions* **240**, 243–260.

Lynch EM, **Kollman JM and Webb BA** (2020) Filament formation by metabolic enzymes-A new twist on regulation. *Current Opinion in Cell Biology* **66**, 28–33.

Maki-Yonekura S, **Yonekura K and Namba K** (2010) Conformational change of flagellin for polymorphic supercoiling of the flagellar filament. *Nature Structural & Molecular Biology* **17**, 417–422.

Meng EC, Goddard TD, Pettersen EF, Couch GS, Pearson ZJ, Morris JH and Ferrin TE (2023) UCSF ChimeraX: Tools for structure building and analysis. *Protein Science* **32**, e4792.

Merino F, Pospich S, Funk J, Wagner T, Kullmer F, Arndt HD, Bieling P and Raunser S (2018) Structural transitions of F-actin upon ATP hydrolysis at near-atomic resolution revealed by cryo-EM. *Nature Structural & Molecular Biology* **25**, 528–537.

Mishra S (2023) Emerging trends in cryo-EM-based structural studies of neuropathological amyloids. *Journal of Molecular Biology* **435**, 168361.

Montemayor EJ, Ploscariu NT, Sanchez JC, Parrell D, Dillard RS, Shebelut CW, Ke Z, Guerrero-Ferreira RC and Wright ER (2021) Flagellar structures from the bacterium *Caulobacter crescentus* and implications for phage ϕCbK predation of multiflagellin bacteria. *Journal of Bacteriology* **203**, e00399–20.

Nakane T, Kotecha A, Sente A, McMullan G, Masiulis S, Brown P, Grigoras IT, Malinauskaite L, Malinauskas T, Miehling J, Uchanski T, Yu L, Karia D, Pechnikova EV, de Jong E, Keizer J, Bischoff M, McCormack J, Tiemeijer P, Hardwick SW, Chirgadze DY, Murshudov G, Aricescu AR and Scheres SHW (2020) Single-particle cryo-EM at atomic resolution. *Nature* **587**, 152–156.

Nedeljkovic M, Kreutzberger MAB, Postel S, Bonsor D, Xing Y, Jacob N, Schuler WJ, Egelman EH and Sundberg EJ (2023) An unbroken network of interactions connecting flagellin domains is required for motility in viscous environments. *PLoS Pathogens* **19**, e1010979.

Nittolo T, Ravindran A, Gonzalez CF and Ramsey J (2019) complete genome sequence of *Agrobacterium tumefaciens* myophage milano. *Microbiology Resource Announcements* **8**, e0058719.

Noble AJ and de Marco A (2024) Cryo-focused ion beam for in situ structural biology: State of the art, challenges, and perspectives. *Current Opinion in Structural Biology* **87**, 102864.

Park CK and Horton NC (2019) Structures, functions, and mechanisms of filament forming enzymes: A renaissance of enzyme filamentation. *Biophysical Reviews* **11**, 927–994.

Park CK and Horton NC (2020) Novel insights into filament-forming enzymes. *Nature Reviews Molecular Cell Biology* **21**, 1–2.

Pazour GJ, Agrin N, Leszyk J and Witman GB (2005) Proteomic analysis of a eukaryotic cilium. *Journal of Cell Biology* **170**, 103–113.

Pijper A and Abraham G (1954) Wavelengths of bacterial flagella. *Journal of General Microbiology* **10**, 452–456.

Pillay N, Mariotti L, Zaleska M, Inian O, Jessop M, Hibbs S, Desfosses A, Hopkins PCR, Templeton CM, Beuron F, Morris EP and Guettler S (2022) Structural basis of tankyrase activation by polymerization. *Nature* **612**, 162–169.

Poweleit N, Ge P, Nguyen HH, Loo RR, Gunsalus RP and Zhou ZH (2016) CryoEM structure of the *Methanospirillum hungatei* archaellum reveals structural features distinct from the bacterial flagellum and type IV pili. *Nature Microbiology* **2**, 16222.

Punjani A and Fleet DJ (2021) 3D variability analysis: Resolving continuous flexibility and discrete heterogeneity from single particle cryo-EM. *Journal of Structural Biology* **213**, 107702.

Punjani A, Rubinstein JL, Fleet DJ and Brubaker MA (2017) cryoSPARC: Algorithms for rapid unsupervised cryo-EM structure determination. *Nature Methods* **14**, 290–296.

Punjani A, Zhang H and Fleet DJ (2020) Non-uniform refinement: Adaptive regularization improves single-particle cryo-EM reconstruction. *Nature Methods* **17**, 1214–1221.

Reynolds MJ, Hachicho C, Carl AG, Gong R and Alushin GM (2022) Bending forces and nucleotide state jointly regulate F-actin structure. *Nature* **611**, 380–386.

Samatey FA, Imada K, Nagashima S, Vonderviszt F, Kumasaka T, Yamamoto M and Namba K (2001) Structure of the bacterial flagellar protofilament and implications for a switch for supercoiling. *Nature* **410**, 331–337.

Sanchez JC, Montemayor EJ, Ploscariu NT, Parrell D, Baumgardt JK, Yang JE, Sibert B, Cai K and Wright ER (2023) Atomic-level architecture of *Caulobacter crescentus* flagellar filaments provide evidence for multi-flagellin filament stabilization. *BioRxiv*.

Scheres SH (2020) Amyloid structure determination in RELION-3.1. *Acta Crystallographica Section D: Structural Biology* **76**, 94–101.

Scheres SHW (2012) RELION: Implementation of a Bayesian approach to cryo-EM structure determination. *Journal of Structural Biology* **180**, 519–530.

Scheres SHW, Ryskeldi-Falcon B and Goedert M (2023) Molecular pathology of neurodegenerative diseases by cryo-EM of amyloids. *Nature* **621**, 701–710.

Schwab J, Kimanius D, Burt A, Dendooven T and Scheres SHW (2024) DynaMight: Estimating molecular motions with improved reconstruction from cryo-EM images. *Nature Methods* **21**, 1855–1862.

Shibata S, Matsunami H, Aizawa SI and Wolf M (2019) Torque transmission mechanism of the curved bacterial flagellar hook revealed by cryo-EM. *Nature Structural & Molecular Biology* **26**, 941–945.

Sonani RR, Bianco S, Dietrich B, Doutch J, Draper ER, Adams DJ and Egelman EH (2024a) Atomic structures of naphthalene dipeptide micelles unravel mechanisms of assembly and gelation. *Cell Reports Physical Science* **5**, 101812.

Sonani RR, Palmer LK, Esteves NC, Horton AA, Sebastian AL, Kelly RJ, Wang F, Kreutzberger MA, Russell WK and Leiman PG (2024b) An extensive disulfide bond network prevents tail contraction in *Agrobacterium tumefaciens* phage Milano. *Nature Communications* **15**, 756.

Sonani RR, Sanchez JC, Baumgardt JK, Kundra S, Wright ER, Craig L and Egelman EH (2023) Tad and toxin-coregulated pilus structures reveal unexpected diversity in bacterial type IV pili. *Proceedings of the National Academy of Sciences* **120**, e2316668120.

Sun M, Azumaya CM, Tse E, Bulkley DP, Harrington MB, Gilbert G, Frost A, Southworth D, Verba KA, Cheng Y and Agard DA (2021) Practical considerations for using K3 cameras in CDS mode for high-resolution and high-throughput single particle cryo-EM. *Journal of Structural Biology* **213**, 107745.

Tamborrini D, Wang Z, Wagner T, Tacke S, Stabrin M, Grange M, Kho AL, Rees M, Bennett P, Gautel M and Raunser S (2023) Structure of the native myosin filament in the relaxed cardiac sarcomere. *Nature* **623**, 863–871.

Trachtenberg S, DeRosier DJ, Aizawa S and Macnab RM (1986) Pairwise perturbation of flagellin subunits. The structural basis for the differences between plain and complex bacterial flagellar filaments. *Journal of Molecular Biology* **190**, 569–576.

Trachtenberg S, DeRosier DJ and Macnab RM (1987) Three-dimensional structure of the complex flagellar filament of *Rhizobium lupini* and its relation to the structure of the plain filament. *Journal of Molecular Biology* **195**, 603–620.

Trachtenberg S, DeRosier DJ, Zemlin F and Beckmann E (1998) Non-helical perturbations of the flagellar filament: *Salmonella typhimurium* SJW117 at 9.6 A resolution. *Journal of Molecular Biology* **276**, 759–773.

Valentine RC, Shapiro B and Stadtman E (1968) Regulation of glutamine synthetase. XII. Electron microscopy of the enzyme from *Escherichia coli*. *Biochemistry* **7**, 2143–2152.

Wakabayashi K and Mitsui T (1970) An X-ray diffraction study of reconstituted straight *Salmonella* flagella. *Journal of Molecular Biology* **53**, 567–570.

Wang F, Burrage AM, Postel S, Clark RE, Orlova A, Sundberg EJ, Kearns DB and Egelman EH (2017) A structural model of flagellar filament switching across multiple bacterial species. *Nature Communications* **8**, 960.

Wang F, Gnewou O, Solemanifar A, Conticello VP and Egelman EH (2022) Cryo-EM of helical polymers. *Chemical Reviews* **122**, 14055–14065.

Wang YA, Yu X, Yip C, Strynadka NC and Egelman EH (2006) Structural polymorphism in bacterial EspA filaments revealed by cryo-EM and an improved approach to helical reconstruction. *Structure* **14**, 1189–1196.

Weis F and Hagen WJH (2020) Combining high throughput and high quality for cryo-electron microscopy data collection. *Acta Crystallographica D Structural Biology* **76**, 724–728.

Wirth R (2012) Response to Jarrell and Albers: Seven letters less does not say more. *Trends in Microbiology* **20**, 511–512.

Yonekura K, Maki-Yonekura S and Namba K (2003) Complete atomic model of the bacterial flagellar filament by electron cryomicroscopy. *Nature* **424**, 643–650.

Zhang R, Alushin GM, Brown A and Nogales E (2015) Mechanistic origin of microtubule dynamic instability and its modulation by EB proteins. *Cell* **162**, 849–859.

Zhang X and Mahamid J (2024) Protocol for subtomogram averaging of helical filaments in cryo-electron tomography. *STAR Protocols* **5**, 103272.

Zhong ED, Bepler T, Berger B and Davis JH (2021) CryoDRGN: Reconstruction of heterogeneous cryo-EM structures using neural networks. *Nature Methods* **18**, 176–185.